A Broadband Circularly Polarized Fabry-Perot Resonant Antenna Using A Single-Layered PRS for 5G MIMO Applications

NIAMAT HUSSAIN[ID], MIN-JOO JEONG, JIWOONG PARK, AND NAM KIM[ID]

Department of Computer and Communication Engineering, Chungbuk National University, Cheongju 28644, South Korea

Corresponding author: Nam Kim (namkim@chungbuk.ac.kr)

ABSTRACT This paper presents the design and the realization of broadband circularly polarized (CP) Fabry–Perot resonant antenna using a single superstrate for the fifth-generation (5G) wireless multiple-input-multiple-output (MIMO) applications. The antenna consists of a corner cut patch with a diagonal slot and a superstrate. The individual resonances of the corner cut patch and patch with diagonal slot are overlapped to improve the intrinsic narrow impedance and axial ratio (AR) bandwidths of the single-fed patch antennas. A half-wavelength spaced superstrate having a half-wavelength thickness is employed as a partially reflecting surface (PRS) for high gain and wide AR as well as impedance bandwidths. The design procedure and mechanisms of the PRS are discussed in detail through the equivalent circuit and ray tracing analysis. Simulated and measured results show that the proposed antennas have a wide operational bandwidth of 25–33 GHz (27.6%) for $|S_{11}| < -10$ dB with a stable gain achieving a maximum value of 14.1 dBiC and a wide 3-dB AR bandwidth ranging from 26–31.3 GHz (17%). This operational bandwidth of the antenna covers the proposed entire global 5G millimeter wave (mmWave) spectrum (26–29.5 GHz). Moreover, a 2 × 2 MIMO antenna is designed using the proposed antenna in such a way that the polarization diversity of the adjacent radiator is exploited, resulting in high isolation between antenna elements and low-envelope correlation coefficient, which makes it a suitable candidate for future 5G MIMO applications.

INDEX TERMS Fifth-generation (5G), millimeter wave, MIMO antenna, Fabry-Perot resonant antenna.

I. INTRODUCTION

The congestion, limited bandwidth, and restricted channel capacity of the current wireless system have pushed researchers and engineers to utilize an unused millimeter wave (mmWave) spectrum in the fifth-generation (5G) of wireless communication systems [1]. The upcoming 5G technology is not only promised to meet the exponentially increasing demands of high data rates, reliability, and low power consumption for the massive growth in the number of connected devices around us, but also capable of unlocking the full capabilities of the emerging technologies such as smart cities, virtual reality, and automotive cars [2]. These 5G systems are likely to have several base stations, massive MIMO, and beamforming antennas. The antenna design is one of the key factors to realize mmWave based 5G communication. America and Canada have proposed a 5G mmWave band of 27.5 – 28.35 GHz, while the United Kingdom and most of the European countries (Finland, Sweden, Italy, Spain, etc.) have suggested 26.5 – 27.5 GHz band, and Korea and Japan have been considering 26.5 – 29.5 GHz and 27.5 – 29.5 GHz bands, respectively [3]. Various studies have been carried out on designing antennas for these potential mmWave bands [4]–[38]. The antenna designs with low gain [4]–[6] are not appropriate, because 5G radio waves have the high propagation and atmospheric losses with low penetration power due to which signal gets weak while reaching from transmitting to the receiving ends. To address the attenuation factor, high gain antenna arrays [7]–[11] and arrays with beam-steering capabilities have been widely studied to increase the signal strength and to provide large spatial coverage [12]–[15]. Even arrays consisting of many radiating elements possess the same capacity as a single antenna being fed with the single port. Thus, the design of high gain antennas maintaining low-profile should be considered, as opposed to the arrays which have inevitable

The associate editor coordinating the review of this manuscript and approving it for publication was Danping He.

losses in power divider networks. These high gain antennas could be the Fabry-Perot cavity antennas [16]–[20], metasurface/metamaterial antennas [21], [22] or lens-coupled antennas [23]. The main disadvantage associated with these antennas is being incapable of MIMO performances. The use of MIMO antennas both in the transmitter and receiver ends provides multiple possible paths for signal transmission enhancing data rate, capacity, and link reliability without additional power and bandwidth, which are the key features of 5G, as presented in the literature [24]–[29]. These MIMO antennas have a good performance exhibiting low mutual coupling but have low gain characteristics (gain < 8 dBic) and are linearly polarized.

On the other hand, one of the promising features of the antenna is circular polarization (CP), wherein the antenna radiates electromagnetic (EM) waves in two orthogonal directions. These kinds of antennas show more immunity to interferences, multipath distortions, and fading than linearly polarized (LP) antennas [30]. Also, CP antennas provide better mobility and orientation freedom between transmitting and receiving antennas, since these antennas radiate in two directions with the same magnitude, while LP antennas radiate in only one direction. This is the reason why circular polarization is popular for wireless and satellite communications, particularly in randomly oriented RFID tags, wireless sensors, and device-to-device communications. Only a few studies have been carried out on CP antennas operating at designated 5G mmWaves bands [31]–[38], especially the CP antennas with MIMO capabilities, even though the CP antennas for 5G spectrum are widely embraced. This is simply because of the design and realization challenges that are associated with the much smaller physical size of the antenna. Though the designs presented in some studies [31]–[36] offer circular polarization, they are single port antennas and are not capable of MIMO performance.

Two designs operating at 5G mmWave bands have been reported to-date, that have both circular polarization and MIMO functionalities [37], [38]. The antenna presented in [37] consists of 2 × 2 aperture coupled microstrip patch antennas and two-layered FSS superstrate. The CP was achieved by circular patch exited by cross-shaped slots, while the FSS superstrate was used to improve antenna performance especially the diversity. Although this design shows an effective approach to mitigate near-field coupling and a good impedance bandwidth of 19.3 % (28 – 33 GHz), it has disadvantages of design and fabrication complexity (two PCBs and two FSS superstrates) and a 6 % narrow AR bandwidth (29.2 – 31 GHz). Interestingly, the superstrate contributed to only a 1.5 dB increment in the gain of the antenna while it degraded the axial ratio (AR) performance, since it was used primarily for improving isolation between antenna elements. In addition, this design needs the optimization of several design parameters of complicated FSS unit cells with multi-layered substrates. This makes it quite difficult to design and mass production and thus practical applications are limited. Another CP antenna with MIMO

configuration [38] is a dual-band multi-polarized system for the base station and has the ability to provide linear and CP signals according to the assigned user's equipment polarization. Nevertheless, the targeted application for this design is the base station, the vivaldi antenna array was distributed in upside conical frustum configuration with the excitation of twelve ports and the single antenna showed a 6% impedance bandwidth and an AR bandwidth of less than 3% (27.5 – 28.5 GHz) with a maximum gain of 8 dBic at 28 GHz band. Although it has multi-polarization and dual-band advantages, this antenna system has low gain and narrow band characteristics. Accordingly, designing of a compact, low-cost, high gain, and circularly polarized MIMO antenna with broadband operation covering the whole allocated mmWave spectrum (25GHz – 29.5 GHz) for future 5G systems would be an important step on the road in the realization of 5G wireless systems.

Starting from these considerations, the design of a broadband circularly polarized antenna with MIMO capabilities based on a Fabry-Perot resonant cavity at mmWave 5G frequency bands is proposed in this paper. The main motivation of this work is to design a high gain, and broadband CP antenna to covers the whole allocated mmWave 5G spectrum from 25 – 33 GHz with good MIMO capabilities. A half-wavelength spaced single-layered dielectric slab having a half-wavelength thickness is utilized as a partially reflecting surface (PRS) for high gain characteristics and wider AR as well as impedance bandwidths. The proposed 2 × 2 MIMO antenna has a simple design and a compact overall size of $1.58\lambda_L \times 1.58\lambda_L \times 0.7\lambda_L$ (λ_L is the free space wavelength of the lowest operating frequency in -10 dB bandwidth) enabling its easy integration with 5G smart devices along with low-cost and mass-production suitability. In addition, this design is unique simply because it is the only one currently available CP MIMO antenna covering the mmWave band (26 – 29.5 GHz) proposed for future 5G applications.

The paper is organized as follows. Section II explains the antenna operation principle based on ray tracing analysis and transmission line mode. The single CP antenna geometry, design methodology, and results are discussed in Section III. Meanwhile, the 2 × 2 element MIMO antenna and its performance characteristics along with the comparison of the proposed design with other designs are explained in Section IV. Finally, our conclusions are drawn in Section V.

II. DESIGN OF THE COMPACT WIDEBAND SINGLE-LAYERED PRS

It is well known that the conventional Fabry-Perot (FP) cavity can be formed by stacking a partially reflective surface (PRS) at a half-wavelength distance above the conducting ground plane. The actual distance between the ground and PRS is determined by their reflection phases at the resonance frequency. The EM waves in this cavity may be excited by any radiating source, such as dipole, horn, waveguide, or a patch. Conventionally, the bandwidth of the FP cavity is increased by achieving a reflection phase of PRS that changes

slowly against the frequency. This kind of reflection phase can be obtained using FSS superstrates [18] by optimizing several design parameters of complex FSS unit cells. This is why the use of unprinted PRSs are getting popular in the design of FP cavity antennas [40]. Although the antenna profile can be reduced using a printed PRS having a quarter-wavelength thickness in mmWave bands, these designs suffer from narrow 3-dB gain bandwidth [17]–[20], especially the AR bandwidth in CP antennas [18], [37]. The analysis of the FP cavity is based on multiple-interference of the radiations emitted by the radiator inside the cavity as shown in Fig. 1.
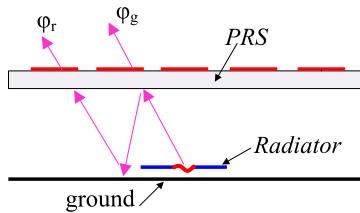

FIGURE 1. Radiation mechanism of the Fabry-Perot cavity antennas.

According to ray tracing analysis, the maximum broadside radiation would be obtained at resonance frequency f_{res}, when the reflected waves from the ground plane are in phase with the reflection phase of PRS. Thus, the resonant condition of this FP cavity having a thickness of h_T (distance from ground plan to PRS) can be expressed as:

$$h_T = \frac{c}{4\pi f_{res}} \left(\varphi_r + \varphi_g - 2N\pi \right), \quad N = 0, 1, 2, 3, \ldots \quad (1)$$

Here, c is the speed of light, φ_r is the reflection phase of the PRS, and φ_g is the reflection phase of the ground plane. To maintain a low-profile, usually the first resonance is considered ($N = 0$) and the properties of the PRS can be tuned by adjusting the reflection phase of PRS.

Since both φ_r and h_T are frequency sensitive, the PRS has narrowband characteristics. Furthermore, the maximum directivity increases with the reflection amplitude of the PRS, while the 3-dB gain bandwidth decreases [37]. Therefore, the realization of a wideband operation maintaining high gain characteristics is a challenge in the design of FP cavity antennas. Considering $\varphi_g = \pi$ for a perfectively electric conducting ground plane, the above equation (1) can be written as:

$$\varphi_r = \frac{4\pi h_T}{c} f_{res} + (2N - 1)\pi, \quad N = 0, 1, 2, 3, \ldots \quad (2)$$

This shows that a wideband resonance can be realized by using a PRS whose reflection phase increases with the increasing frequency. A typical phase response of the PRS for broadband performance [16] and the phase (φ_r for narrowband which decreases against frequency for narrowband [18], is shown in Fig. 2.

The phase for narrowband PRS intersects with the ideal phase (φ_g) only at a single frequency resulting in a narrowband characteristic, while the wideband PRS may resonate
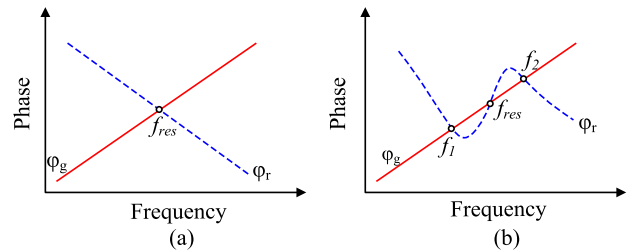

FIGURE 2. Phase response of a typical PRS: (a) Narrowband operation and (b) broadband operation.

at three different frequencies, since the phase cuts the ideal phase curve at three different points ($f_1, f_{res}, \& f_2$).

In our design, we choose a PRS with a half-wavelength ($0.5\lambda_{sub}$) thickness after simulating PRS with different thickness values. A separation between the PRS and the ground is set to be around half-wavelength, in accordance to the conventional FP cavity design rules. The proposed PRS is composed of a high dielectric constant material Rogers 6010 ($\varepsilon_r = 10.2$, $tan\delta = 0.0026$) having a thickness of $h_a = 1.6$ mm, which corresponds to the half-wavelength ($0.5\lambda_{PRS}$), where λ_{PRS} is the wavelength in the PRS at the resonance frequency of 28 GHz.

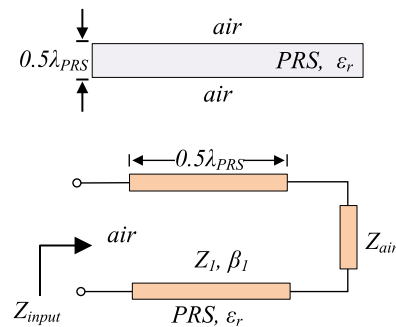For a physical insight, the PRS can be modeled to its equivalent circuit diagram as shown in Fig. 3.

FIGURE 3. The proposed PRS and its equivalent transmission model.

The reflection response (Γ_{PRS}) of the PRS can be computed from the input impedance Z_{input}.

$$Z_{input} = Z_1 \frac{Z_{air} + jZ_1 + tan\beta h_{PRS}}{Z_1 + jZ_{air} + tan\beta h_{PRS}} \quad (3)$$

Here Z_{air} is the characteristic impedance of air, Z_1 is the characteristic impedance of PRS which is equal to ($Z_1 = Z_{air}/\sqrt{\varepsilon_r}$ and β is the phase constant ($\beta = 2\pi \sqrt{\varepsilon_r}/\lambda_0$) in the PRS and ε_r is the relative primitivity. The Γ_{PRS} can be calculated as:

$$\Gamma_{PRS} = \frac{Z_{input} - Z_{air}}{Z_{input} + Z_{air}} \quad (4)$$

We computed the phase (Γ_{PRS}) characteristics of the designed PRS ($ha = 1.6$ mm and $h_T = 5.5$mm) through a superstrate reflection model (SRM) and the ideal phase curve
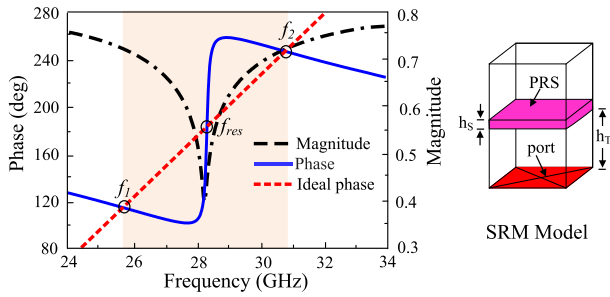
FIGURE 4. Simulated reflection phase and magnitude of the proposed PRS using SRM model.

FIGURE 5. Geometry of the proposed single-element antenna: (a) Front view and (b) side view.

was obtained with the help of (2) as shown in Fig. 4. The proposed FP cavity shows a nearly zero-reflection phase magnitude $|\Gamma_{PRS}|$ around the resonance frequency of 28 GHz and resulted in a 180° phase jump of the reflection phase. When the frequency switches its polarity at a certain condition of $|\Gamma_{PRS}| = 0$, the real and imaginary components of the phase reverse their signs. This provides a phase change of 180°. This phenomenon is responsible for intersecting the ideal phase (φ_r line in three points namely f_1, f_{res}, and f_2. This shows that the FP cavity has the potential to resonate with high gain characteristics around these three intersecting frequencies based on (1). It should be mentioned that similar phase response to that of our proposed design have been recently obtained for closely spaced multi-layered PRS in microwave frequencies [39]–[41], which allows for a wider broadside radiation bandwidth.

In summary, a high gain and wideband FP cavity is designed by using single-layered PRS with a half-wavelength thickness for the antenna design at 5G mmWave frequencies.

III. DESIGN AND CHARACTERIZATION OF THE SINGLE-ELEMENT ANTENNA

This section explains the geometry, design methodology, and characterization of a single-element broadband circularly polarized Fabry-Perot resonant antenna. First, an optimized single antenna is modeled by tuning design parameters and then its characteristics are discussed based on simulation and experimental results.

A. ANTENNA CONFIGURATION

The geometry and configuration of the single antenna is shown in Fig. 5. The antenna consists of a corner cut square patch with a diagonal slot and a single-layered dielectric slab above the patch at a separation of h_T.

The patch's width and length are defined as w, and is etched on the Rogers 5880 ($\varepsilon_r = 2.2$, $tan\delta = 0.0009$, $h = 0.508 \, mm$). The corners of the patch are truncated by t to achieve CP performance. A diagonal slot which has length L and width s is used to improve impedance and AR bandwidths. The dielectric slab is used as a PRS for overall performance enhancement of the antenna. The PRS is made up of high dielectric constant material Rogers 6010 ($\varepsilon_r = 10.2$,
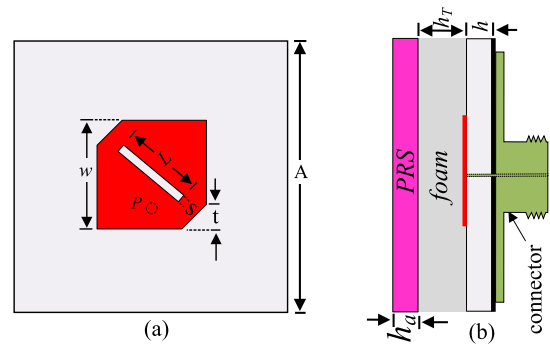
$tan\delta = 0.0023$) has a thickness h_S. The antenna is fed with 2.92mm K-connector at position $P(0, 1.2)$, by connecting the inner pin of the connector to the patch while connecting the outer conductor to the ground. The optimized designed parameters of the antenna are: $A = 10$ mm, $w = 3.2$ mm, $h = 0.508$ mm, $t = 0.85$ mm, $L = 1$ mm, $s = 0.2$ mm, $h_T = 5.5$ mm, and $h_a = 1.6$ mm.

B. ANTENNA DESIGN PROCEDURE

The proposed antenna design begins with the simulation of a simple rectangular patch antenna in commercial simulator CST Microwave Studio. For ease of realization at high frequencies and to minimize the connector effects, the patch is directly fed by SMA without any extended strip line by compromising the bandwidth of the antenna [42]. The patch dimensions are then optimized so that the antenna resonates at the central frequency of 28 GHz. Since the rectangular patch gives a linear polarization, the corners of the patch are truncated to get circular polarization. Later, a diagonal slot is etched on the patch for both impedance and AR bandwidth enhancement. Principally, in single-fed patch antennas, CP is achieved by slightly perturbing patch geometry at the right position with respect to the feeding point. The perturbation technique includes truncated corners, stubs, slits, notches, and embedded slot onto the patch. The most common and convenient way to get CP radiation is truncating a set of patch corners or inserting a diagonal slot in the patch such that two orthogonal modes of the same magnitude are simultaneously excited [43]. This design combines both conventional techniques (a truncated corner patch and a patch with a diagonal slot) to improve AR as well as impedance matching by overlapping the individual resonances of the patch with diagonal slot and truncated patch. The impedance matching in terms of reflection loss $|S_{11}|$, AR, and broadside gain for different antenna configurations are shown in Fig. 6. The truncated patch antenna (Ant.#1) exhibits an expected narrow impedance and AR bandwidths of 7.8 % and 2.5%, respectively, while the patch with a diagonal slot (Ant.#2) shows a similar performance except for a shift of resonance to the lower frequencies. In fact, the slot provides a longer effective path for current flow, hence the resonance is shifted down to
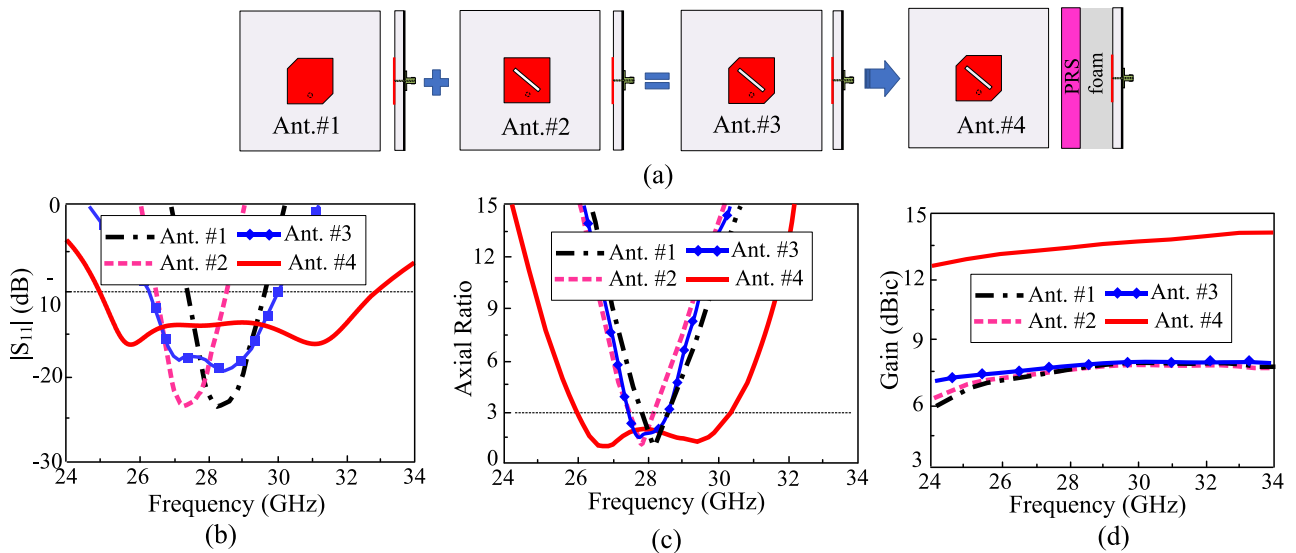
FIGURE 6. d Antennas configurations and their characteristics: (a) antennas geometry, (b) |S₁₁|, (c) axial ratio, and (d) broadside gain.

the lower frequencies. The truncated patch antenna with an optimized diagonal slot (Ant.#3), which is the combination of antenna #1 and #2, shows significant improvement in $|S_{11}|$ and AR bandwidths by overlapping the individual resonances of the slot and truncated patch. More specifically, the $|S_{11}|$ and AR bandwidths of Ant.#3 is almost the sum of the bandwidths of Ant.#1 and Ant.#2. Finally, the previously designed $0.5\lambda_{sub}$ thick PRS at a separation of half-wavelength above the patch antenna (Ant.#3) is stacked for overall performance enhancement of the patch antenna. The patch antenna with PRS shows a massive improvement up to 27.6 % and 18.5 % for impedance and AR bandwidths, respectively. It is important to note that the broadside gain for patch antenna configurations without PRS is 7.5 dBi, this increased to 14.1 dBic for patch antenna with PRS. The performance comparison of these antennas is summarized in Table 1. The detailed mechanism of performance improvement due to PRS is well described in [39]. Hence, the proposed single-element Fabry-Perot cavity antenna design is completed. The step-wise design approach and optimization procedure using key design parameters of the single antenna are illustrated with the help
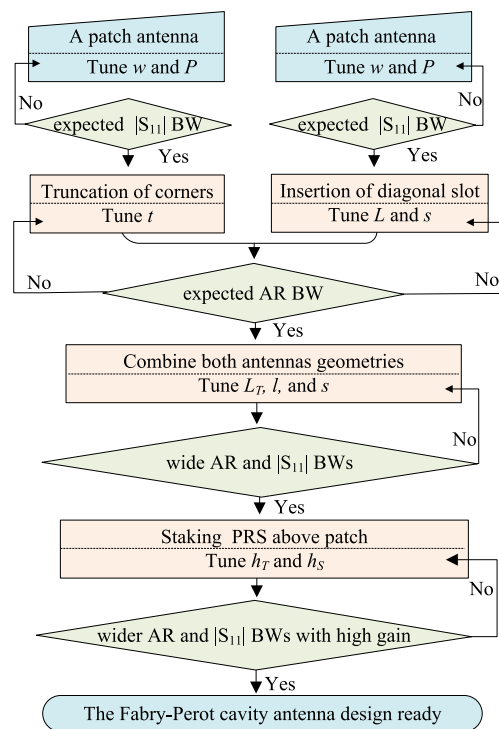

FIGURE 7. The flowchart describing the design procedure and optimization process of the proposed single-element antenna (BW=bandwidth).

of the flowchart in Fig. 7. It is clear from the flowchart that how the antenna is designed and what parameters are used to optimize the specific antenna characteristics.

C. RESULTS AND DISCUSSION

The characteristics of the proposed antenna in terms of reflection loss ($|S_{11}|$), axial ratio, broadside gain, and radiation

TABLE 1. Performance comparison far the different antenna configurations.

Antennas	-10 dB |S₁₁| bandwidth	3-dB AR bandwidth	Max. Gain
Ant.#1	7.8 % (27 − 29.2 GHz)	2.5 % (27.8 − 28.5 GHz)	7.5 dBic
Ant.#2	7.5 % (26.9 − 29 GHz)	2.5% (27.4 − 28.1 GHz)	7.5 dBic
Ant.#3	14 % (26.1 − 30 GHz)	4.3 % (27.4 − 28.6 GHz)	7.5 dBic
Ant.#4	27.6 % (25 − 33 GHz)	18.5 % (26 − 31.3 GHz)	14.1 dBic

patterns are investigated numerically and validated with measured results. For the fabrication of the prototype, we choose a commercially available high-frequency substrate Rogers RO5880 with a thickness of 20 mil (0.508 mm). The antenna is fabricated by JDM Co. Ltd., Ansan-si, Korea with standard PCB technologies. The air gap between the radiator and the PRS is realized carefully using a polyurethane foam of the desired thickness. The inner part of foam was truncated to avoid losses in the foam, while the antenna was fed by 2.92 mm K-connector. The photographs of fabricated prototype and parts for antenna assembly are shown in Fig. 8.
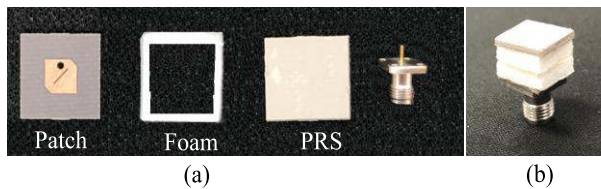

FIGURE 8. Photos of the fabricated single-element antenna: (a) parts for assembly and (b) side view of the fabricated prototype.

The antenna far-field measurements are carried out in the anechoic chamber at the Electromagnetic Wave Technology Institute, Seoul, Korea. A well-calibrated dual-ridged horn antenna (18 – 40 GHz) is employed as the source antenna while the fabricated prototype is measured as the receiving antenna. Transmit and receiver amplifier are used to provide stable power reception. The data obtained from the dual-linear polarized horn antenna are analyzed to calculate the CP radiations of the antenna.
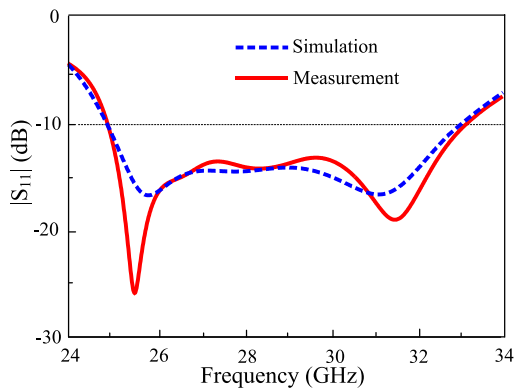

FIGURE 9. Return loss $|S_{11}|$ of the proposed single-element antenna as a function of frequency.

Fig. 9 shows the simulated and measured $|S_{11}|$ of the antenna. The antenna exhibited broadband characteristics by demonstrating a simulated wide -10 dB impedance bandwidth ranging from 25 – 33 GHz, which is a little wider than its measured value. This discrepancy is most likely due to cable losses and fabrication tolerances. These wideband characteristics are associated with the overlapping of the slot and truncated patch resonances and successful implementation of the well-designed single-layered PRS.
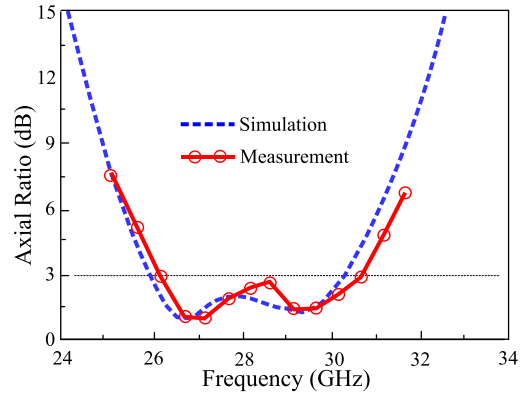

FIGURE 10. The axial ratio of the proposed single-element antenna as a function of frequency.

The axial ratio of the antenna as a function of frequency is given in Fig. 10. The AR can be computed in Fabry-Perot antennas as in [37]:

$$AR(dB) = 10 \log \left| \frac{\left| \vec{E}_\theta + j\vec{E}_\phi \right|}{\left| \vec{E}_\theta + j\vec{E}_\phi \right|} + \frac{\left| \vec{E}_\theta - j\vec{E}_\phi \right|}{\left| \vec{E}_\theta - j\vec{E}_\phi \right|} \right| \quad (5)$$

Here $E_\ominus$ and E_φ are the electric field components, whose phases are changed due the to the air gap ($h_T = 5.5$ mm) between the radiator and the PRS. It is noted that the proposed antenna shows a broadband 3-dB axial ratio of 18.5 % (26 – 31.3 GHz), yielding two minimum AR points with AR values of 0.5 dB and 1 dB around 26.5 GHz and 29.5 GHz, respectively. Again, the broadband AR characteristic is primarily due to the PRS as well as the combination of individual AR bandwidths of truncated and slotted patch as explained previously (Fig. 6). It is worth noting that the proposed antenna operational CP bandwidth covers the entire global 5G mmWave spectrum (26 – 29.5 GHz). The difference between measured and simulated AR values are quite reasonable and are possibly due to the imperfections of the PRS position above the patch since a foam is used to realize the separation between patch and PRS.

Fig. 11 compares the measured and simulated broadside gain of the proposed single-element antenna with PRS and simulated gain of the antenna without PRS. The antenna without PRS attained an expectedly low gain of 7 dBic as other patch antennas. However, the antenna with PRS demonstrated high and stable gain characteristics with a minimum and a maximum value of 12.7 dBic and 14.1 dBic at 25 GHz and 33 GHz, respectively. The gain slightly increased with the increasing frequency due to the increased effective size of the antenna at higher frequencies. The measured results agree well with its counterpart with a little decrement. This could be due to the substrate losses and the power dissipation in the foam (used to realize the cavity thickness). The patch, in conjunction with the well-designed PRS, enables the multiple reflections between the radiator and the PRS providing multiple images of the radiator that increasing the antenna
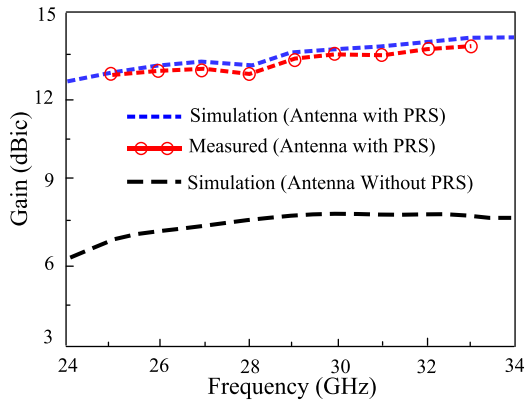
FIGURE 11. Broadside gain of the single-element antenna with and without PRS as a function of frequency.

gain substantially. To verify this observation, we computed the electric field (E-field) distributions of the antenna with and without PRS in xz and yz-plane in Fig. 12. The PRS acted as a lens for focusing the E-field of the antenna in broadside direction resulting in a noticeable enhancement for the antenna gain.
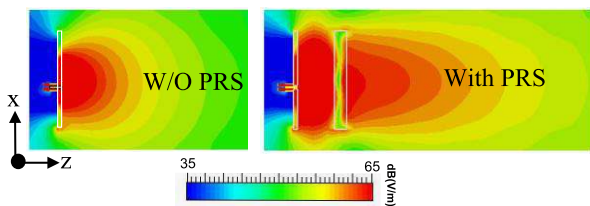

FIGURE 12. Simulated electric field distributions of the antenna with and without (W/O) PRS.

The radiation patterns of the fabricated prototype of the antenna is simulated and measured at different frequencies and are illustrated in Fig. 13. The radiation pattern is symmetrical at both the principal planes of xz-plane (H-plane) and yz-plane (E-plane), which almost remained the same for all investigated frequencies. Such outcomes indicate high stability of the far-field patterns along the entire pass-band. The left-hand circular polarization (LHCP) is minor when compared to the right-hand circular polarization (RHCP), thus the proposed antenna has RHCP radiations. This can be further validated by E-field direction in PRS seen from the $+z$-direction (Fig. 14). It can be clearly observed that the radiated field from the radiator rotates in a counter-clockwise direction, verifying the antenna has RHCP.

IV. DESIGN AND CHARACTERIZATION OF MIMO ANTENNA

The single-element Fabry-Perot cavity antenna is incorporated into a four-element MIMO assembly to exploit multipath propagation to enhanced data rate, capacity and link reliability for its applications in future 5G MIMO systems. The geometry and performance of the MIMO antenna is
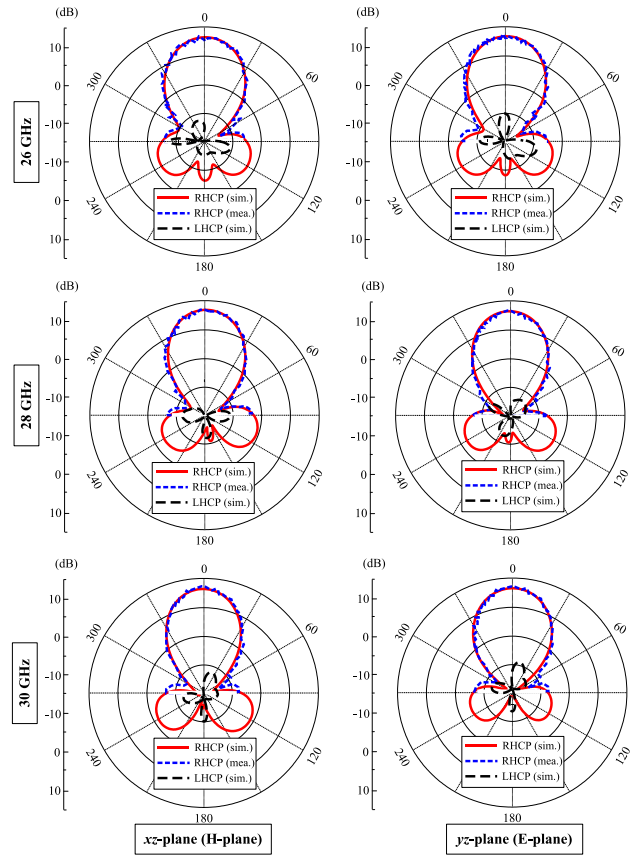

FIGURE 13. Radiation patterns of the proposed single-element antenna at different frequencies.
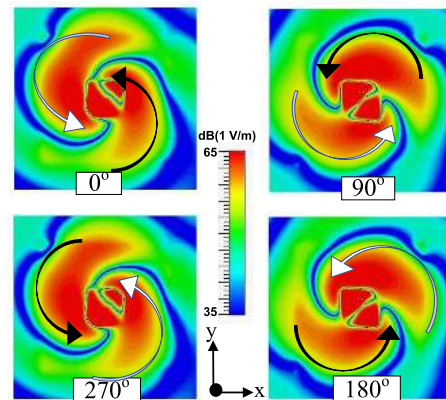
FIGURE 14. The E-field variations for different phase values seen from +z-direction of the antenna.

further investigated based on return loss, isolation between the antenna elements, and envelope correlation coefficient and individual gain of the MIMO antennas.

A. ANTENNA CONFIGURATION

The proposed MIMO consists of two-by-two single-element antennas arranged perpendicular to each other with a spacing of $D = 8$ mm as shown in Fig. 15. The conventional MIMO design suggests a minimum element spacing of $\lambda_0/2$, which

FIGURE 15. Geometry of the proposed MIMO antenna: (a) Top view of patch antennas and (b) side view of antenna.
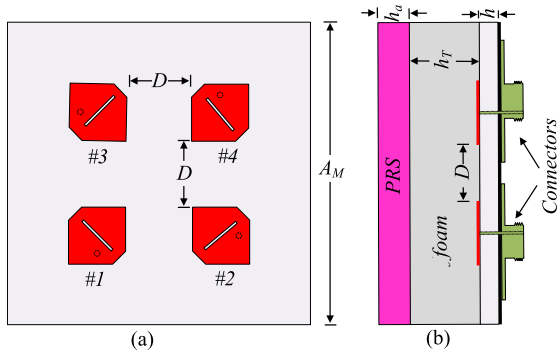

FIGURE 17. Return loss $|S_{11}|$ of the proposed MIMO antennas as a function of frequency.

FIGURE 18. Isolation between the proposed MIMO antennas in terms of reflection coefficient as a function of frequency.

is equal to 5.4 mm at the central frequency of 28 GHz. Based on the dimensions of the 2.92 mm K-connector, this spacing is deliberately increased to 8 mm, so that the connectors could fit well on the shared substrate. The placement of all antennas has been done in a shared substrate, having a dimension of $A_M \times A_M \times h$ mm^3. Moreover, a single slab of the dielectric is placed over a separation of h_T. In the design of MIMO, only the length of substrate and PRS *A* is increased to $A_M = 19$ mm, while all other parameters including the substrate and PRS thickness remain the same as the single-element antenna. Since the antenna is composed of two substrates, the proposed MIMO offers a low-cost mass production suitability besides of its overall compact size of $1.58\lambda_L \times 1.58\lambda_L \times 0.7\lambda_L$.

B. RESULTS AND DISCUSSION

The proposed 2×2 MIMO antenna is fabricated and tested to validate the simulation results (Fig. 16). A polyurethane foam is used to realize the optimized separation between antennas and PRS.
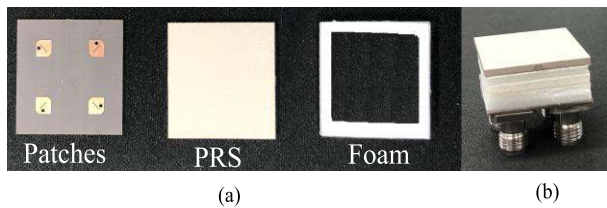

FIGURE 16. Photos of the fabricated 2 x 2 MIMO antenna: (a) parts for MIMO assembly and (b) side view of the fabricated prototype.

The measured and simulated reflection loss curves for only antenna #1 and #4 are plotted in Fig. 17, since all antennas are identical and have symmetrical placement. It can be observed that the antennas #1 and #4 have almost the same values of reflection loss. The MIMO antennas exhibited the same -10 dB impedance bandwidth (25 – 33 GHz) as the single-element antenna, however, there is a small difference in the curve shape because of the increased length of substrate and PRS in the MIMO configuration.
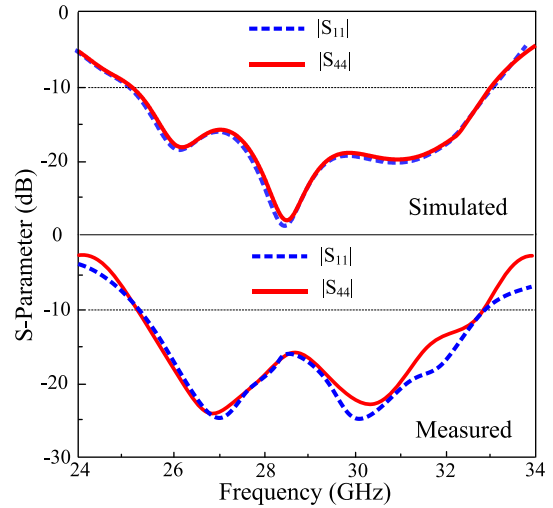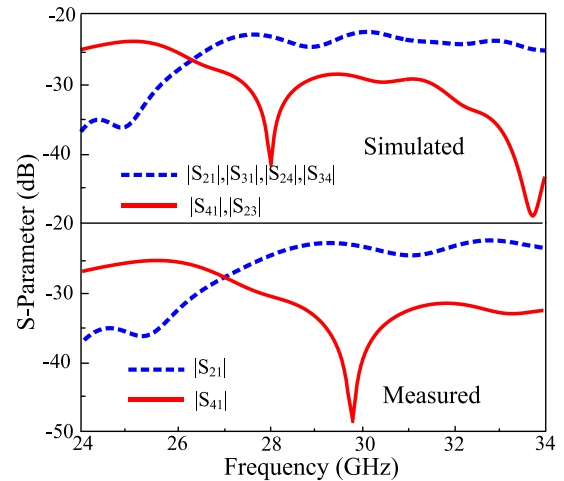
The isolation between antenna elements of the proposed MIMO system is plotted in terms of S-Parameter (Fig. 18). Since all the antennas are identical and are symmetrically placed perpendicular to each other in a square substrate, the simulated curves for $|S_{21}|$, $|S_{31}|$, $|S_{24}|$, and $|S_{34}|$ are same with an isolation of more than 25 dB in the entire frequency bandwidth. However, the simulated results of $|S_{41}|$ and $|S_{23}|$ are identical to each other and showed better isolation (<30 dB) performance than the former ones. In fact, the distance between antenna #4 and antenna #1 is the same as the antennas are in diagonal position. Moreover, the distance between the antennas located at the diagonal positions is larger than the distance among the neighboring antennas which resulted in higher average isolation of 35 dB in the operational bandwidth. The measured results of the $|S_{21}|$ and $|S_{41}|$ showed a good agreement with the simulated results. The parameter which shows the MIMO performance of the
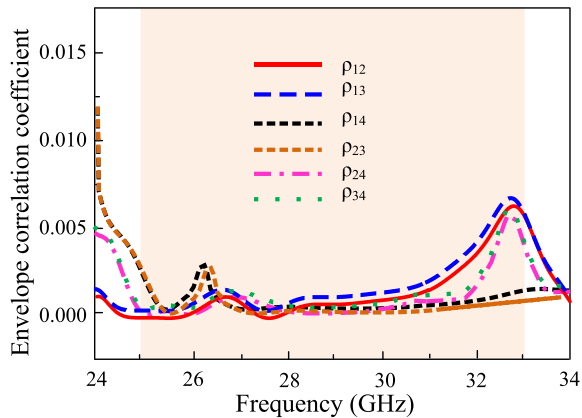
FIGURE 19. Envelope correlation coefficient for the proposed MIMO antennas for 5G applications.

TABLE 3. Comparison of the proposed antenna with previous works.

Ref. Antennas	Antenna Type	f_c (GHz)	No. of Ports	LP/ CP	AR BW (%)	$|S_{11}|$ BW (%)	Max. Gain (dBic)
[17]	Fabry-Perot	28	01	LP	-	8.9	16
[18]	Fabry-Perot	30	01	CP	2.9	8.2	15
[19]	Fabry-Perot	28	01	LP	-	15.5	15.4
[26]	Patch	28	04	LP	-	11	7.4
[27]	Patch	31	04	LP	-	39	10.6
[28]	Patch	25.2	08	LP	-	15.6	8.7
[29]	Dipole	28	04	LP	-	17.5	10
[36]	Cross-dipole	28	01	CP	8	8	2.2
[37]	Fabry-Perot	30	04	CP	5	5	8
[38]	Vivaldi	28/38	12	CP/LP	3	6	8
Proposed	Fabry-Perot	28	04	CP	17	27.6	14.1

antennas is the envelope correlation coefficient (ρ_e). It determines how MIMO antennas are independent in their individual performance, including the radiation pattern, antenna polarization, diversity gain, and phase between the antennas in the MIMO system. Fig. 19 shows the numerically calculated ρ_e for the antennas for the set of antennas using (5), as in [25], [26].

$$\rho_e = \frac{\left| S_{12}S_{11}^* + S_{22}S_{21}^* \right|^2}{\left[1 - \left(|S_{11}|^2 + |S_{21}|^2 \right) \right] \left[1 - \left(|S_{22}|^2 + |S_{21}|^2 \right) \right]} \quad (6)$$

The peak values of ρ_e are smaller than 0.008 in the desired range of frequencies, which is much smaller than the practically acceptable value referring to the excellent diversity performance of the proposed antenna.

The simulated and measured gains of each antenna in the proposed MIMO assembly is depicted in Table 2. During the measurement of antenna 1, only port 1 is exited while the remaining ports were terminated with 50-Ω load. Similarly, the measurements of the rest of the antennas are carried out by only exiting the respective antenna port and connecting other ports with the 50-Ω load. The values of gain for all antennas are almost the same and are similar to the single-element antenna investigated earlier in Section III. This endorses the good diversity characteristics as well as the stability of the far-field patterns of the MIMO antennas.

TABLE 2. Measured and simulated gains of the MIMO antennas.

Freq. (GHz)	Gain (dBic) of Antenna Element No.							
	Simulated values				Measured values			
	#1	#2	#3	#4	#1	#2	#3	#4
25	12.7	12.6	12.6	12.6	12.5	12.4	12.4	12.5
27	13.5	13.4	13.5	13.5	13.2	13.2	13.2	13.3
29	13.9	13.9	14	13.8	13.6	13.6	13.6	13.7
31	14.0	14.0	13.9	13.8	13.8	13.8	13.8	13.7
33	14.1	13.9	14.1	14.0	14.0	13.9	13.8	14.0

Finally, the performance of the proposed 5G MIMO antenna is compared with some other recently reported mmWave antennas ([17]–[19], [26]–[29], and [36]–[38])

in Table 3. Most of the MIMO antennas in the 5G mmWave band are linearly polarized except [37] and [38]. The CP antennas with the key advantages of MIMO functionalities presented in [37], [38] have the disadvantages of design complexity besides of its narrow $|S_{11}|$ and AR bandwidths, as well as low gain characteristics. Moreover, the proposed antenna outperformed the existing Fabry-Perot antennas ([17]–[19] and [37]) irrespective of their polarization due to its comparable gain (14.1dBic) and very wide operational bandwidth. In summary, none of the designs combine the advantages of simpler design, high gain, broadband CP characteristics, and MIMO capabilities at one package as our proposed design does. Moreover, our design is unique simply because it is the only one currently available CP MIMO antenna that covers the mmWave band (26 – 29.5 GHz) proposed for future 5G applications.

V. CONCLUSION

A high-gain and broadband circularly polarized (CP) Fabry-Perot resonant antenna utilizing a single-layered PRS is presented for 5G MIMO applications. The proposed single-element antenna is composed of a corner cut patch with a diagonal slot and a single-layered PRS. The two conventional CP designs (corner cut patch and diagonal slotted patch) are combined to overcome the intrinsic narrow impedance and axial ratio (AR) bandwidths of the single-feed patch antennas. A half-wavelength thick PRS is placed above the antenna for high gain and broadband characteristics. Simulated and measured results show that the proposed antennas have a wider -10 dB bandwidth of 25 – 33 GHz (27.6 %) with a maximum gain of 14.1 dBic, and a wide 3-dB AR bandwidth ranging from 26 – 31.3 GHz. This operational bandwidth of the antenna covers the 5G mmWave spectrum (26 – 29.5 GHz) proposed by most of the countries. Performance of the single-element antenna is further investigated for a 2 × 2 MIMO system which shows an excellent diversity performance owing to its high isolation between antenna elements and low envelope correlation coefficients. These characteristics make the proposed antenna as a good candidate for 5G MIMO applications.

REFERENCES

[1] J. Thompson *et al.*, "5G wireless communication systems: Prospects and challenges," *IEEE Commun. Mag.*, vol. 52, no. 2, pp. 62–64, Feb. 2014.

[2] T. S. Rappaport *et al.*, "Millimeter wave mobile communications for 5G cellular: It will work!" *IEEE Access*, vol. 1, pp. 335–349, 2013.

[3] Qualcomm Technologies Inc. (Dec. 2017). *Spectrum for 4G and 5G*. Accessed: Jan. 5, 2019. [Online]. Available: https://www.qualcomm.com/news/media-center

[4] Y. Yashchyshyn *et al.*, "28 GHz switched-beam antenna based on S-PIN diodes for 5G mobile communications," *IEEE Antennas Wireless Propag. Lett.*, vol. 17, no. 2, pp. 225–228, Feb. 2018.

[5] M.-C. Tang, T. Shi, and R. W. Ziolkowski, "A study of 28 GHz, planar, multilayered, electrically small, broadside radiating, huygens source antennas," *IEEE Trans. Antennas Propag.*, vol. 65, no. 12, pp. 6345–6354, Dec. 2017.

[6] X. Lin, B.-C. Seet, F. Joseph, and E. Li, "Flexible fractal electromagnetic bandgap for millimeter-wave wearable antennas," *IEEE Antennas Wireless Propag. Lett.*, vol. 17, no. 7, pp. 1281–1285, Jul. 2018.

[7] N. Yoon and C. Seo, "A 28-GHz wideband 2×2 U-slot patch array antenna," *J. Electromagn. Eng. Sci.*, vol. 17, no. 3, pp. 133–137, 2017.

[8] J. Kim, S. C. Song, H. Shin, and, Y. B. Park, "Radiation from a millimeter-wave rectangular waveguide slot array antenna enclosed by a von karman radome," *J. Electromagn. Eng. Sci.*, vol. 18, no. 3, pp. 154–159, 2018.

[9] P. A. Dzagbletey and Y. B. Jung, "Stacked microstrip linear array for millimeter-wave 5G baseband communication," *IEEE Antennas Wireless Propag. Lett.*, vol. 17, no. 5, pp. 780–783, May 2018.

[10] Y. Li and K.-M. Luk, "Wideband perforated dense dielectric patch antenna array for millimeter-wave applications," *IEEE Trans. Antennas Propag.*, vol. 63, no. 8, pp. 3780–3786, Aug. 2015.

[11] B. Biglarbegian, M. Fakharzadeh, D. Busuioc, M.-R. Nezhad-Ahmadi, and S. Safavi-Naeini, "Optimized microstrip antenna arrays for emerging millimeter-wave wireless applications," *IEEE Trans. Antennas Propag.*, vol. 59, no. 5, pp. 1742–1747, May 2011.

[12] Z. Briqech, A.-R. Sebak, and T. A. Denidni, "Low-cost wideband mm-Wave phased array using the piezoelectric transducer for 5G applications," *IEEE Trans. Antennas Propag.*, vol. 65, no. 12, pp. 6403–6412, Dec. 2017.

[13] J. Bang and J. Choi, "A SAR reduced mm-Wave beam-steerable array antenna with dual-mode operation for fully metal-covered 5G cellular handsets," *IEEE Antennas Wireless Propag. Lett.*, vol. 17, no. 6, pp. 1118–1122, Jun. 2018.

[14] A. H. Naqvi and S. Lim, "Review of recent phased arrays for millimeter-wave wireless communication," *Sensors*, vol. 18, no. 10, p. 3194, 2018.

[15] B. Yu, K. Yang, C.-Y.-D. Sim, and G. Yang, "A novel 28 GHz beam steering array for 5G mobile device with metallic casing application," *IEEE Trans. Antennas Propag.*, vol. 66, no. 1, pp. 462–466, Jan. 2018.

[16] H. Attia, M. L. Abdelghani, and T. A. Denidni, "Wideband and high-gain millimeter-wave antenna based on FSS Fabry–Pérot cavity," *IEEE Trans. Antennas Propag.*, vol. 65, no. 10, pp. 5589–5594, Oct. 2017.

[17] O. M. Haraz, A. Elboushi, S. A. Alshebeili, and A.-R. Sebak, "Dense dielectric patch array antenna with improved radiation characteristics using EBG ground structure and dielectric superstrate for future 5G cellular networks," *IEEE Access*, vol. 2, pp. 909–913, 2014.

[18] M. Akbari, S. Gupta, M. Farahani, A. R. Sebak, and T. A. Denidni, "Gain enhancement of circularly polarized dielectric resonator antenna based on FSS superstrate for MMW applications," *IEEE Trans. Antennas Propag.*, vol. 64, no. 12, pp. 5542–5546, Dec. 2016.

[19] M. Asaadi, I. Afifi, and A.-R. Sebak, "High gain and wideband high dense dielectric patch antenna using FSS superstrate for millimeter-wave applications," *IEEE Access*, vol. 6, pp. 38243–38250, 2018.

[20] L. Leger, T. Monediere, and B. Jecko, "Enhancement of gain and radiation bandwidth for a planar 1-D EBG antenna," *IEEE Microw. Wireless Compon. Lett.*, vol. 15, no. 9, pp. 573–575, Sep. 2005.

[21] M. J. Al-Hasan, T. A. Denidni, and A. R. Sebak, "Millimeter-wave EBG-based aperture-coupled dielectric resonator antenna," *IEEE Trans. Antennas Propag.*, vol. 61, no. 8, pp. 4354–4357, Aug. 2013.

[22] N. Hussain and I. Park, "Performance of multiple-feed metasurface antennas with different numbers of patch cells and different substrate thicknesses," *Appl. Comput. Electromagn. J.*, vol. 33, no. 1, pp. 49–55, 2018.

[23] L. Mall and R. B. Waterhouse, "Millimeter-wave proximity-coupled microstrip antenna on an extended hemispherical dielectric lens," *IEEE Trans. Antennas Propag.*, vol. 49, no. 12, pp. 1769–1772, Dec. 2001.

[24] A. A. R. Saad and H. A. Mohamed, "Printed millimeter-wave MIMO-based slot antenna arrays for 5G networks," *AEU-Int. J. Electron. Commun.*, vol. 99, pp. 59–69, Feb. 2019.

[25] B. Yang, Z. Yu, Y. Dong, J. Zhou, and W. Hong, "Compact tapered slot antenna array for 5G millimeter-wave massive MIMO systems," *IEEE Trans. Antennas Propag.*, vol. 65, no. 12, pp. 6721–6727, Dec. 2017.

[26] J. S. Park, J.-B. Ko, H.-K. Kwon, B.-S. Kang, B. Park, and D. Kim, "A tilted combined beam antenna for 5G communications using a 28-GHz band," *IEEE Antennas Wireless Propog. Lett*, vol. 15, pp. 1685–1688, 2016.

[27] S. F. Jilani and A. Alomainy, "Millimetre-wave T-shaped MIMO antenna with defected ground structures for 5G cellular networks," *IET Microw., Antennas Propag.*, vol. 12, no. 5, pp. 672–677, Apr. 2018.

[28] N. Shoaib, S. Shoaib, R. Y. Khattak, I. Shoaib, X. Chen, and A. Perwaiz, "MIMO antennas for smart 5G devices," *IEEE Access*, vol. 6, pp. 77014–77021, 2018.

[29] Z. Wani, M. P. Abegaonkar, and S. K. Koul, "A 28-GHz antenna for 5G MIMO applications," *Prog. Electromagn. Res. Lett.*, vol. 78, pp. 73–79, Aug. 2018.

[30] K. M. Mak, H. W. Lai, K. M. Luk, and C. H. Chan, "Circularly polarized patch antenna for future 5G mobile phones," *IEEE Access*, vol. 2, pp. 1521–1529, 2014.

[31] Y. Yao, X. Cheng, C. Wang, J. Yu, and X. Chen, "Wideband circularly polarized antipodal curvedly tapered slot antenna array for 5G applications," *IEEE J. Sel. Areas Commun.*, vol. 35, no. 7, pp. 1539–1549, Jul. 2017.

[32] X. Cheng, Y. Yao, J. Yu, and X. Chen, "Circularly polarized substrate-integrated waveguide tapered slot antenna for millimeter-wave applications," *IEEE Antennas Wireless Propag. Lett.*, vol. 16, pp. 2358–2361, 2017.

[33] K. R. Mahmoud and A. M. Montaser, "Design of dual-band circularly polarised array antenna package for 5G mobile terminals with beam-steering capabilities," *Microw., Antennas Propag.*, vol. 12, no. 1, pp. 29–39, Jan. 2017.

[34] Q. Wu, J. Hirokawa, J. Yin, C. Yu, H. Wang, and W. Hong, "Millimeter-Wave multibeam endfire dual-circularly polarized antenna array for 5G wireless applications," *IEEE Trans. Antennas Propagat.*, vol. 66, no. 9, pp. 4930–4935, Sep. 2018.

[35] S.-J. Park and S.-O. Park, "LHCP and RHCP substrate integrated waveguide antenna arrays for millimeter-wave applications," *IEEE Antennas Wireless Propag. Lett.*, vol. 16, pp. 601–604, 2017.

[36] W. Lin, R. W. Ziolkowski, and T. C. Baum, "28 GHz compact omnidirectional circularly polarized antenna for device-to-device communications in the future 5G systems," *IEEE Trans. Antennas Propag.*, vol. 65, no. 12, pp. 6904–6914, Dec. 2017.

[37] M. Akbari, H. A. Ghalyon, M. Farahani, A.-R. Sebak, and T. A. Denidni "Spatially decoupling of CP antennas based on FSS for 30-GHz MIMO systems," *IEEE Access*, vol. 5, pp. 6527–6537, 2017.

[38] K. R. Mahmoud and A. M. Montaser, "Synthesis of multi-polarised upside conical frustum array antenna for 5G mm-Wave base station at 28/38 GHz," *IET Microw., Antennas Propag.*, vol. 12, no. 9, pp. 1559–1569, 2018.

[39] N. Wang, L. Talbi, Q. Zeng, and J. Xu, "Wideband Fabry–Pérot resonator antenna with electrically thin dielectric superstrates," *IEEE Access*, vol. 6, pp. 14966–14973, 2018.

[40] N. Nguyen-Trong, H. H. Tran, T. K. Nguyen, and A. M. Abbosh, "A compact wideband circular polarized Fabry–Pérot antenna using resonance structure of thin dielectric slabs," *IEEE Access*, vol. 6, pp. 56333–56339, 2018.

[41] N. Nguyen-Trong, H. H. Tran, T. K. Nguyen, and A. M. Abbosh, "Wideband Fabry–Pérot antennas employing multilayer of closely spaced thin dielectric slabs," *IEEE Antennas Wireless Propag. Lett.*, vol. 17, no. 7, pp. 1354–1358, Jul. 2018.

[42] W. Yang, J. Zhou, Z. Yu, and L. Li, "Single-fed low profile broadband circularly polarized stacked patch antenna," *IEEE Trans. Antennas Propag.*, vol. 62, no. 10, pp. 5406–5410, Oct. 2014.

[43] P. C. Sharma and K. C. Gupta, "Analysis and optimized design of single feed circularly polarized microstrip antennas," *IEEE Trans. Antennas Propag.*, vol. AP-31, no. 6, pp. 949–955, Nov. 1983.

NIAMAT HUSSAIN received the B.S. degree in electronics engineering from the Dawood University of Engineering and Technology, Karachi, Pakistan, in 2014, and the M.S. degree in electrical and computer engineering from Ajou University, Suwon, South Korea. He is currently pursuing the Ph.D. degree in information and communication engineering with Chungbuk National University, Chungju-si, South Korea. His research interests include lens-coupled antennas, metasurface antennas, metamaterial antennas, UWB antennas, mmWave antennas, and terahertz antennas. He was bestowed with best paper award in 2017, for his paper presented at Korea Winter Conference.

JIWOONG PARK received the bachelor's degree in electronics engineering from Chungbuk National University, South Korea, in 2017, where he is currently pursuing the master's degree with the Department of Information and Communication Engineering. His research interests include EMC, antenna design for WIFI, and mobile communication.

MIN-JOO JEONG received the B.S. degree in electronics engineering from Chosun University, in 2013, and the M.S. degree in LED fusion engineering from Pukyong National University, South Korea, in 2015. He is currently pursuing the Ph.D. degree in information and communication engineering with Chungbuk National University, Chungju-si, South Korea. His research interests include EMC, antenna design, and EMF.

NAM KIM received the B.S., M.S., and Ph.D. degrees from Yonsei University, Seoul, South Korea, in 1981, 1983, and 1988, respectively, all in electronics engineering. He has been a Professor with the School of Information and Communication Engineering, Chungbuk National University, Chengju, South Korea, since 1989. His scientific interests include optical information processing, the health effect of the EMF, wireless power transfer, and antennas for mobile communications. He is a member of the International Advisory Committee for the World Health Organization project on EMF, the IEEE International Committee on Electromagnetic Safety, and the International Electro Technical Commission TC 106. He was the President of the Bioelectromagnetics Society.

• • •